PHYSICAL REVIEW FLUIDS **10**, 124805 (2025)

Dynamics of a neutrally buoyant sphere during oblique water exit

Yang Huang,[1] Qing Xiao,[1,*] and Qiang Zhu[2]
[1]*Department of Naval Architecture, Ocean and Marine Engineering, University of Strathclyde,*
Glasgow G4 0LZ, Scotland, United Kingdom
[2]*Department of Structural Engineering, University of California, La Jolla, San Diego, California 92093, USA*

(Received 26 August 2025; accepted 17 November 2025; published 30 December 2025)

Understanding the water exit dynamics of solid bodies is of fundamental importance for trans-medium vehicles, projectiles, and other ocean engineering applications. The water exit of a neutrally buoyant sphere is investigated using large-eddy simulation combined with an overset mesh technique. The sphere is launched from a fixed depth with varying initial velocities and launch angles. The results reveal distinct features of velocity attenuation, rotational response, and trajectory deflection. The critical exit velocity exhibits a nonlinear dependence on the launch angle (θ_0). The exit process consists of two stages: in the fully submerged phase, the relative velocity loss decreases with increasing initial velocity, whereas in the partially submerged phase, the loss approaches a θ_0-dependent constant. The sphere undergoes rotation whose magnitude converges to a θ_0-dependent limit, with the rotation direction switching from clockwise to counterclockwise as θ_0 increases. Lateral trajectory deflection occurs in most cases, except at $\theta_0 = 0^\circ$ and 45°, and is primarily governed by the interaction between the shed vortices and the free surface together with the image effect. Secondary contributions, including the sphere's rotation and asymmetric wave-induced pressure distribution, amplify the deflection magnitude but do not alter its direction. These findings provide new physical insight into the mechanisms of water exit and underscore the critical role of launch conditions, with implications for predicting and controlling the motion and stability of underwater vehicles, projectiles, and marine structures.

DOI: 10.1103/xj4j-jtkl

I. INTRODUCTION

The water exit of submerged bodies is a canonical multiphase problem with broad implications in both engineering and biology. In marine applications, it governs the recovery of submersibles, the performance of unmanned aerial-underwater vehicles (UAUVs), and the deployment of deep-sea mining systems [1–4]. In nature, species such as flying fish and archer fish exploit rapid water exit to escape from predators or capture prey, inspiring amphibious robotic designs [5,6]. Under these contexts, the exit process involves strong water-air-solid body interactions, free-surface rupture, cavity formation, droplet entrainment, and unsteady hydrodynamic loading, all of which make prediction and control highly challenging [7–10].

---

[*] Contact author: qing.xiao@strath.ac.uk

Experimental investigations have provided fundamental insights into the dynamics of water exit for canonical geometries. For spheres launched vertically, it has been shown that the Reynolds number of the near-wake flow becomes nearly invariant with immersion depth, and the maximum rise height is systematically lower than inviscid predictions due to viscous dissipation and surface-energy work [11,12]. High-speed visualizations reveal rich interfacial phenomena, including droplet adhesion, ligament formation, and film breakup, all of which act as channels of energy loss [12–15]. Truscott *et al.* [8] reported that buoyant spheres display two robust ascent modes: a near-vertical trajectory producing higher jumps, and an oscillatory mode associated with lateral deviations driven by vortex shedding. Takamure and Uchiyama [11,16,17] extended these findings by demonstrating that immersion depth and density ratio alter the post-exit trajectory and redistribute kinetic and potential energy, with deeper release sometimes leading to reduced jump height. More recently, lattice-Boltzmann simulations have revealed that free-surface spike height exhibits strong sensitivity to Froude number below a critical threshold, while becoming weakly dependent above it, and that the subsequent “waterfall” collapse occurs in distinct stages [18].

For cylindrical and other bluff bodies, experiments have shown that hydrodynamic loads during exit are highly sensitive to initial velocity and immersion depth. Systematic tests with vertically launched cylinders reported significant variation in force histories and trajectory stability with small changes in initial conditions, underscoring the difficulty of predicting the timing and magnitude of loads in practical recovery scenarios [13,14,19]. In more complex environments, additional mechanisms arise. For example, exit through brash ice has been observed to generate premature wetting, larger asymmetric loads, and greater attitude errors compared with open-water conditions [20–22]. Similarly, exit in wave environments couples body kinematics with surface elevation, producing strong dependence of exit loads on wave phase and highlighting risks in vehicle recovery under rough seas [3,4]. Together, these experimental findings emphasize that even for simple bodies, exit dynamics remain strongly dependent on initial conditions and environmental forcing.

Meanwhile, analytical and reduced-order models have long been employed to interpret and predict water-exit forces. Extensions of von Kármán-Wagner theory treat the flow as inviscid and irrotational and approximate wetted-area evolution through compatibility conditions, resulting in nonlinear Abel-type integral equations with explicit solutions for simplified two-dimensional and axisymmetric cases [7,10,23]. Within a two-dimensional-plus-time framework, linear theories augmented by compact nonlinear corrections have been shown to reproduce exit forces for slender bodies at shallow draft [7]. Potential-flow boundary-element simulations have advanced these models by explicitly resolving free-surface rupture and body detachment. These studies reveal, for example, that blunter bodies tend to sustain longer interfacial films and generate higher free-surface spikes, and that local force peaks arise shortly before detachment at large Froude numbers [10]. Despite their convenience, such models cannot account for viscous losses, interfacial rupture, or droplet entrainment, all of which play a central role in exit energetics [8,12].

High-fidelity numerical simulations have therefore become indispensable in capturing the nonlinear stages of water exit. Approaches based on the volume-of-fluid (VOF) method, coupled with turbulence models such as large-eddy simulation (LES), have been used to resolve interface deformation, cavity growth, and flow separation around moving bodies [24–26]. Immersed-boundary and overset-grid strategies allow robust treatment of moving bodies with large displacements, enabling systematic studies across wide ranges of parameters. LES of axisymmetric projectiles approaching exit has captured cavity pinch-off and collapse under hydrostatic pressure and shown that nonzero attack angles tilt the air-water interface and trigger asymmetric collapse accompanied by sharp pressure pulses [27]. Ventilated exit simulations and experiments have demonstrated that controlled air injection into the wake cavity can reduce drag, increase vertical speed, and substantially improve attitude stability by mitigating lateral displacement [28–30].

Recent numerical studies have also investigated the effects of environmental complexity. Simulations of exits through brash ice show that cavity shapes become distorted and asymmetric, producing larger lateral loads and longer-lasting oscillations than in open water [21–23]. Exit under waves has been shown to depend strongly on the phase of the incident wave: favourable phasing can reduce exit drag through lift assistance, while unfavourable timing can amplify forces and destabilize trajectories [3,4]. Collectively, these results highlight the effectiveness of CFD in isolating mechanisms that are difficult to be accessed experimentally and reinforce the strong sensitivity of exit dynamics to Froude number, immersion depth, and body orientation [8,11,18,31].

Despite these advances, studies of spheres remain largely restricted to vertical exit, where trajectories remain axisymmetric [8,11,12,18,32]. The influence of oblique launches, characterized by different initial launch angles and velocities, has not been systematically quantified. Key questions remain regarding (i) phase-wise velocity loss, (ii) the coupling between body attitude and free-surface interaction, and (iii) the mechanisms that drive trajectory deflection. Prior observations of lateral oscillations and wake-induced deviation suggest that asymmetric hydrodynamic loading plays a role, but the relationship among rotation, free-surface deformation, and asymmetric pressure fields has not been clearly established.

Our previous work investigated the dynamics and energetics of a neutrally buoyant sphere during vertical exit [32]. That study divided the motion into fully submerged, partially submerged, and airborne phases, and quantified the contributions of viscous forces, radiation effects, gravity, and buoyancy to energy loss. However, the analysis was limited to symmetric vertical trajectories and did not address the oblique exit scenario.

The present study extends this framework by systematically examining the water exit dynamics of a neutrally buoyant sphere launched at different initial velocities and angles. Using large-eddy simulation combined with an overset mesh technique, we investigate (i) velocity attenuation across the fully and partially submerged phases, (ii) attitude evolution including rotation motion, and (iii) trajectory deflection mechanisms. Special attention is given to the role of asymmetric pressure distributions induced by waves and image effect associated with the free surface. By clarifying these features, the study provides new physical insight into the oblique water exit process and contributes to the design of trans-medium vehicles and bio-inspired systems.

The remainder of this paper is organized as follows. Section II introduces the physical problem of sphere water exit, outlining the division into distinct stages and the definition of key parameters. Section III presents the mathematical formulations, including the governing equations, free-surface modeling, overset mesh technique, and numerical algorithm. Section IV details the computational setup, covering the computational domain and initial conditions. Section V reports and discusses the numerical results, focusing on the dynamics of spheres with varying initial velocities and launch angles. Finally, Sec. VI summarizes the main findings and conclusions.

II. PHYSICAL PROBLEM

This study examines the water exit dynamics of a smooth, homogeneous, and neutrally buoyant sphere of diameter D, as illustrated in Fig. 1. To describe the motion, two coordinate systems are employed. The global coordinate system (x, z) is earth-fixed, where the z-axis points vertically upward from the free surface. The body-fixed coordinate system (X, Z) is attached to the sphere and aligned with its principal axes, with the Z-axis initially coincident with the global z-axis. The location of the sphere's center in the global system is denoted by (x_c, z_c).

Initially, the sphere is positioned at $z_c = -4.5D$ and is impulsively launched with an initial velocity U_0 at an oblique angle θ_0. The launch angle θ_0 is defined as the inclination between the velocity vector U_0 and the global z-axis. The motion is restricted to the x-z plane, and rotation about the transverse y-axis is also included.

At the onset, the sphere has no angular velocity ($\omega_0 = 0$) and no initial rotation angle ($\varphi_0 = 0$), such that the body-fixed and global z-axes are initially aligned. Driven by its initial momentum, the sphere rises through the fluid and eventually breaches the free surface.

The overall motion is divided into two stages: Phase 1 (Fully Submerged): the sphere's center travels from $z_c = -4.5\ D$ to $z_c = -0.5\ D$, attaining a velocity U_1 at the end of this stage; Phase 2 (Partially Submerged): the center moves from $z_c = -0.5\ D$ to $z_c = 0.5D$, ultimately reaching an exit velocity U_2.

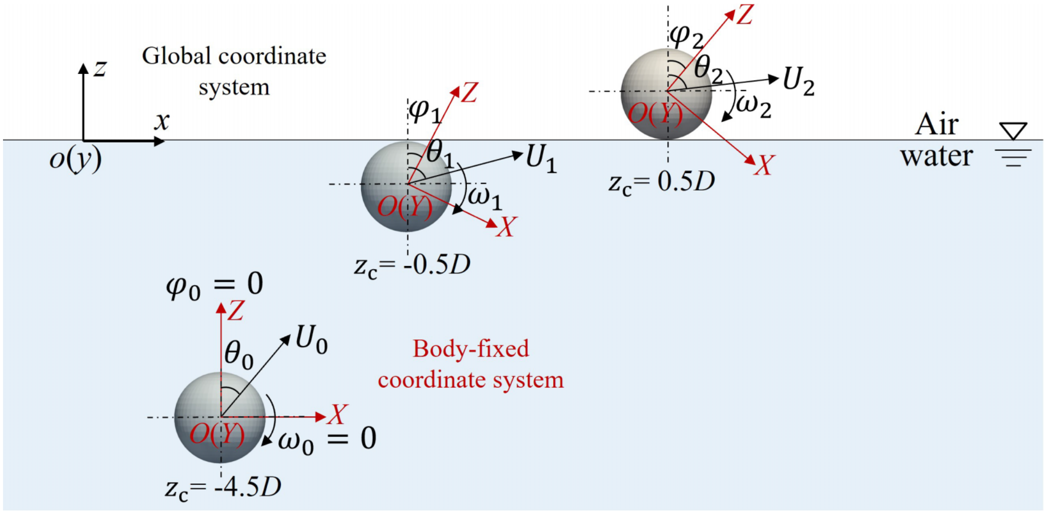

FIG. 1. Schematic of a neutrally buoyant sphere exiting the water with initial velocity U_0 and launch angle θ_0.

III. METHODOLOGY

This study employs a CFD approach based on LES to investigate the water exit process of a sphere. The sphere's motion is modeled using an overset grid technique, which allows accurate resolution of complex boundary movements. The numerical framework has been validated in our previous work [32], where the dynamics and energetics of vertical water exit were thoroughly examined. As such, only a brief overview of the employed methodology is provided below.

A. Governing equations

To simulate the unsteady flow around the sphere during its water exit, LES is employed. The spatially filtered incompressible Navier-Stokes equations governing the fluid domain are expressed as:

$$\frac{\partial \bar{u}_i}{\partial x_i} = 0, \tag{1}$$

$$\frac{\partial \rho \bar{u}_i}{\partial t} + \frac{\partial}{\partial x_j}[\rho \bar{u}_i(\bar{u}_j - \hat{u}_j)] = -\frac{\partial \bar{p}_i}{\partial x_i} + \frac{\partial}{\partial x_j}\left[\mu_e\left(\frac{\partial \bar{u}_i}{\partial x_j} + \frac{\partial \bar{u}_j}{\partial x_i}\right)\right] - \frac{\partial \tau_{ij}}{\partial x_j} + \rho g_i, \tag{2}$$

where x_i are Cartesian coordinates with i corresponding the x, y, and z directions. $\bar{u}_i$ and $\bar{p}_i$ are the filtered velocity and pressure fields, respectively, and $\hat{u}_j$ is the mesh velocity. The effective dynamic viscosity is given by $\mu_e = \rho(\nu + \nu_t)$, where ν and ν_t are the kinematic and eddy viscosities. The gravity acceleration is denoted by g_i.

The subgrid-scale (SGS) stress tensor is defined as

$$\tau_{ij} = \overline{u_i u_j} - \bar{u}_i \bar{u}_j, \tag{3}$$

which represents the effect of the unresolved turbulent motions. It is modeled using the Smagorinsky approach [33]:

$$\tau_{ij} = -2\upsilon_S \bar{S}_{ij}, \tag{4}$$

$$\upsilon_S = (C_s\Delta)^2(2\bar{S}_{ij}\bar{S}_{ij})^{1/2}, \quad \bar{S}_{ij} = \frac{1}{2}\left(\frac{\partial \bar{u}_i}{\partial x_j} + \frac{\partial \bar{u}_j}{\partial x_i}\right), \tag{5}$$

where υ_S is the subgrid-scale eddy viscosity, and $\Delta = (\Delta x \Delta y \Delta z)^{1/3}$ is the local filter width based on grid spacing. The Smargorinsky constant C_s is set as 0.14.

In addition to fluid motion, the translational and rotational dynamics of the sphere are explicitly modeled. The sphere is considered a neutrally buoyant rigid body with two degrees of freedom: translation in the x-z plane and rotation about the y-axis. Its motion follows the Newton-Euler equations:

$$m\frac{d\boldsymbol{U}}{dt} = \boldsymbol{F}_h + \boldsymbol{F}_g, \quad \frac{d}{dt}(\mathbf{I}\boldsymbol{\omega}) = \boldsymbol{T}_h, \tag{6}$$

where $\boldsymbol{U}$ is the velocity of the sphere's center of mass, $\boldsymbol{\omega}$ is the angular velocity vector, m is the mass of the sphere, and $\mathbf{I}$ is its moment of inertia tensor. The hydrodynamic force $\boldsymbol{F}_h$ and torque $\boldsymbol{T}_h$ are obtained by integrating the pressure and viscous stresses over the body surface. The gravitational force is defined as $\boldsymbol{F}_g = m\boldsymbol{g}$, with $\boldsymbol{g}$ being the gravitational acceleration vector.

B. Free surface modeling

The interface between air and water is captured using the VOF method [34]. The scalar field α represents the local volume fraction of water: $\alpha = 1$ denotes pure water, $\alpha = 0$ indicates pure air, and $0 < \alpha < 1$ corresponds to cells containing the interface. The transport equation for α is

$$\frac{\partial \alpha}{\partial t} + \frac{\partial}{\partial x_j}[(\bar{u}_i - \hat{u}_i)\alpha] + \frac{\partial}{\partial x_j}[\bar{u}_{ri}(1-\alpha)\alpha] = 0, \tag{7}$$

where $\bar{u}_{ri}$ is an artificial compression velocity introduced to sharpen the interface. This term is active only near the free surface to maintain a bounded and conservative representation of α.

The local mixture density and viscosity are defined as

$$\rho = \alpha\rho_{\mathrm{w}} + (1-\alpha)\rho_{\mathrm{a}}, \tag{8}$$

$$\mu = \alpha\mu_{\mathrm{w}} + (1-\alpha)\mu_{\mathrm{a}}, \tag{9}$$

where ρ_{w}, ρ_{a}, μ_{w}, and μ_{a} are the densities and dynamic viscosities of water and air, respectively.

C. Dynamic mesh

To accommodate large body motions without excessive mesh distortion, an overset mesh technique is adopted. This approach employs two overlapping grids: a stationary background mesh covering the entire computational domain, and a moving body-fitted mesh that conforms to the geometry of the sphere [35].

The body-fitted mesh follows the rigid-body motion, providing high resolution around the sphere, while the background mesh remains unchanged. The governing equations are solved separately on each mesh, with information exchanged via interpolation across the overlapping region. Although more computationally expensive than traditional deforming meshes, the overset grid method enhances numerical stability and accuracy for simulations involving significant translational or rotational motion, such as water exit.

D. Numerical algorithm

The finite volume method (FVM) is employed to discretize the governing equations. Temporal integration is performed using a second-order Crank-Nicolson scheme, while the convective terms in the Navier-Stokes equations are approximated with a second-order upwind method. Pressure-velocity coupling is achieved using the PIMPLE algorithm, a hybrid approach that combines the pressure implicit with splitting of operators (PISO) method [36] and the semi-implicit method for pressure linked equations (SIMPLE) method [37], thereby improving stability and convergence for

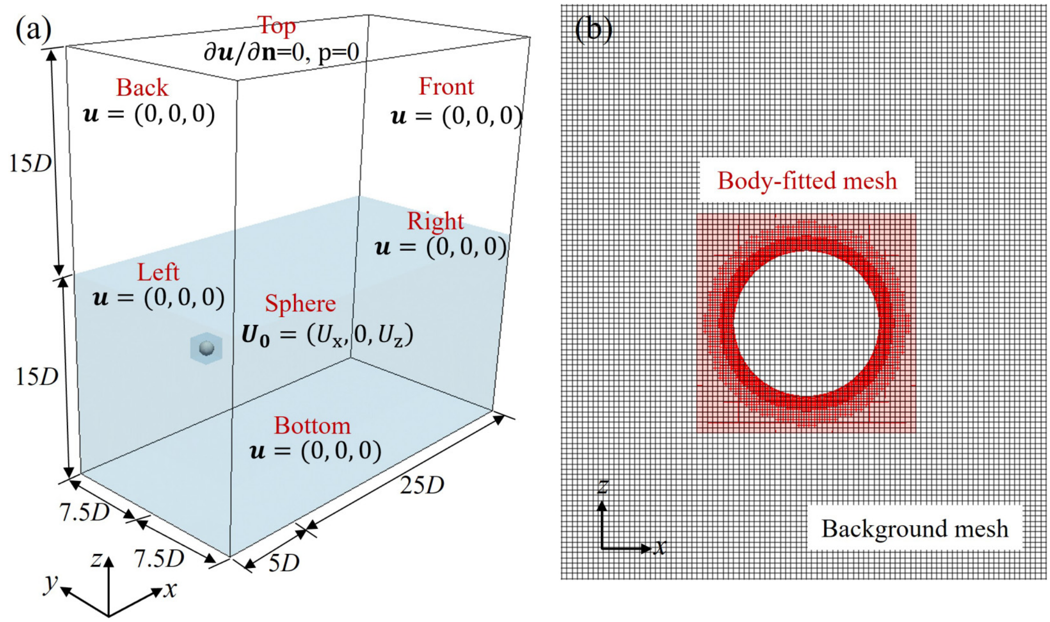

FIG. 2. (a) Computational domain and boundary conditions for the water exit simulation of a sphere; (b) Mesh distribution in the x-z plane.

transient simulations. Spatial gradients are evaluated using a second-order Gauss linear scheme with cell-based limiting.

For the transport equation of the volume fraction field, the multidimensional universal limiter for explicit solution (MULES) algorithm [38–40] is employed. MULES is an explicit solver based on the flux-corrected transport technique, which ensures boundedness of the volume fraction and provides a limited flux for the momentum equation assembly. To reduce numerical diffusion, a second-order upwind scheme is used for the convective terms.

IV. NUMERICAL MODEL

A. Computational domain

The computational domain, illustrated in Fig. 2(a), spans $30D \times 15D \times 30D$ in the Cartesian coordinate system, with a uniform water depth of $15D$. The sphere, with a diameter of $D = 0.2$ m and a density equal to that of water ($\rho_s = \rho_w = 998.2\,\mathrm{kg/m^3}$), is initially positioned at $z_c = -4.5D$. Given the oblique exit trajectory of the sphere from left to right, the horizontal clearances to the left and right boundaries are set to be $5D$ and $25D$, respectively, while the distances to the front and back boundaries are both $7.5D$. During the exit process, the sphere is allowed to undergo translational motion in the x-z plane and rotational motion about the y-axis.

Boundary conditions are specified as follows: the side walls and bottom are treated with no-slip and no-flux conditions, whereas the top surface employs a zero-gradient condition for velocity. These configurations are illustrated in Fig. 2(a), where U_x and U_z denote the sphere's velocity components along the x- and z-axes, respectively. The mesh distribution in the x-z plane is shown in Fig. 2(b). A locally refined body-fitted mesh (red) is employed near the sphere to accurately resolve flow details, while the surrounding domain adopts a coarser background mesh (black) to reduce computational cost.

TABLE I. Initial conditions for the water exit simulations of the sphere.

Vertical position Z	Linear velocity Fr	Angular velocity ω_0 (rad/s)	Launch angle θ_0 (deg)	Rotation angle φ_0 (deg)
−4.5D	$2.1 \sim 8.6$	0	$0 \sim 70$	0

B. Initial conditions for water exit

To explore how the initial velocity and launch angle influence the water exit dynamics of the sphere, a series of simulations is performed under varying initial conditions. The initial velocity is characterized by the Froude number, defined as $Fr = U_0/\sqrt{gD}$, with values ranging from 2.1 to 8.6. The initial launch angle θ_0 varies between 0° and 70°. Based on the sphere's diameter and initial velocity, the corresponding Reynolds number (Re) is $6 \times 10^5 < Re < 2.4 \times 10^6$. Details of all tested initial conditions are summarized in Table I.

V. RESULTS AND DISCUSSIONS

This section presents the results of the water exit dynamics of a sphere subjected to different initial velocities (U_0) and launch angles (θ_0). The discussion begins with convergence tests for both grid resolution and time step size to verify the accuracy and robustness of the numerical simulations. Subsequently, the effects of varying U_0 and θ_0 on the sphere's velocity loss, rotational dynamics, and trajectory deflection during the water exit process are examined. The underlying physical mechanisms governing these dynamic responses are also discussed in detail.

A. Convergence tests

To ensure numerical accuracy, simulations are performed using three grid resolutions. The minimum cell sizes near the sphere, the corresponding surface-averaged y^+, and the total number of cells in each mesh configuration are summarized in Table II. The sphere is initialized with a velocity of $U_0 = 12$ m/s, corresponding to $Fr = 8.6$, and a launch angle of $\theta_0 = 30°$. A time step of $\Delta t = 5 \times 10^{-4}$ s is used in the initial analysis.

It should be noted that the reported y^+ values are relatively large ($120 \sim 240$). This is expected because the present study involves a high-Reynolds-number (2.4×10^6) external flow, where fully resolving the near-wall viscous sublayer is computationally prohibitive. Instead, a wall-modeled LES strategy is adopted, in which maintaining y^+ within the logarithmic layer ($30 \leqslant y^+ \leqslant 300$) is sufficient to capture the correct wall-shear behavior while ensuring computational feasibility [41–43].

In addition, time-step sensitivity is evaluated using $\Delta t = 2.5 \times 10^{-4}$ s, 5×10^{-4} s, and 1×10^{-3} s with the medium resolution mesh. Figure 3 presents the time histories of the sphere's displacement and velocity in the x-z plane for various grid and time step settings. The results show good agreement between the medium and fine meshes, and the simulation with $\Delta t = 5 \times 10^{-4}$ s exhibits negligible deviation from that with $\Delta t = 2.5 \times 10^{-4}$ s. Thus, to balance accuracy and

TABLE II. Grid configurations used in the convergence study.

Mesh type	Minimum grid size	y^+	Total number of grids
Coarse mesh	$0.018D \times 0.018D \times 0.018D$	240	1.81 million
Medium mesh	$0.013D \times 0.013D \times 0.013D$	170	5.13 million
Fine mesh	$0.009D \times 0.009D \times 0.009D$	120	14.5 million

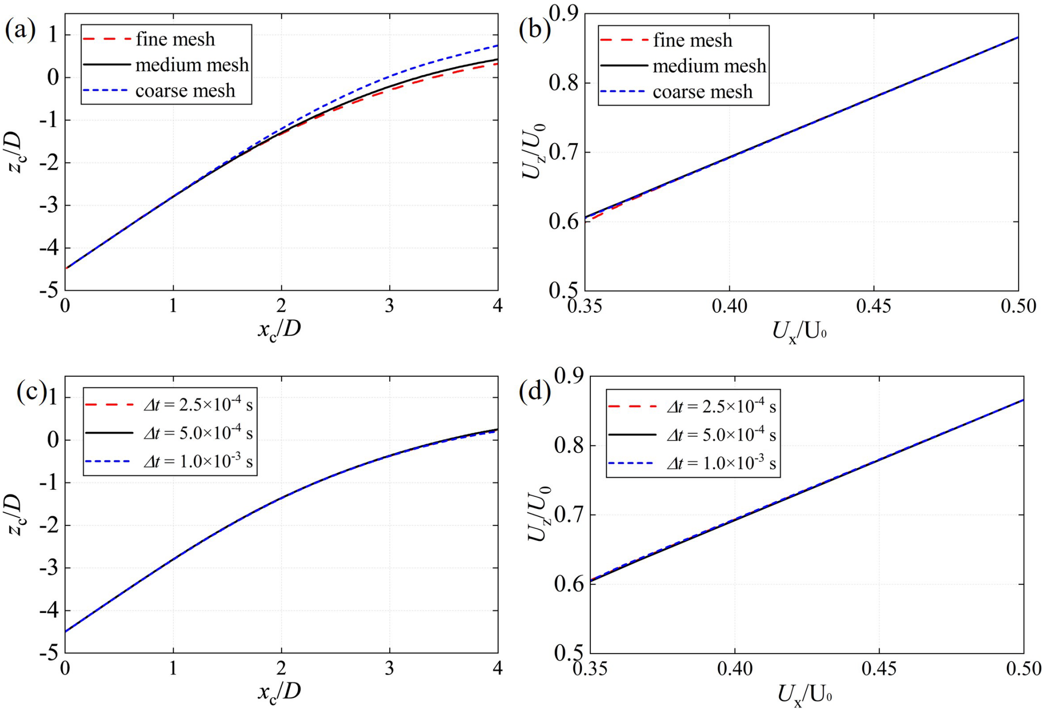

FIG. 3. Time histories of displacement and velocity in the *x*-*z* plane for different mesh resolutions and time steps: (a) displacement (b) and velocity with different meshes; (c) displacement and (d) velocity with different time steps.

computational efficiency, the medium resolution mesh combined with $\Delta t = 5 \times 10^{-4}$ s is adopted for all subsequent simulations.

B. Velocity loss

Figure 4(a) illustrates the water exit configuration. Initially located at $z_c = -4.5D$ below the free surface, the sphere is launched with an initial velocity U_0 and launch angle θ_0. During its ascent,

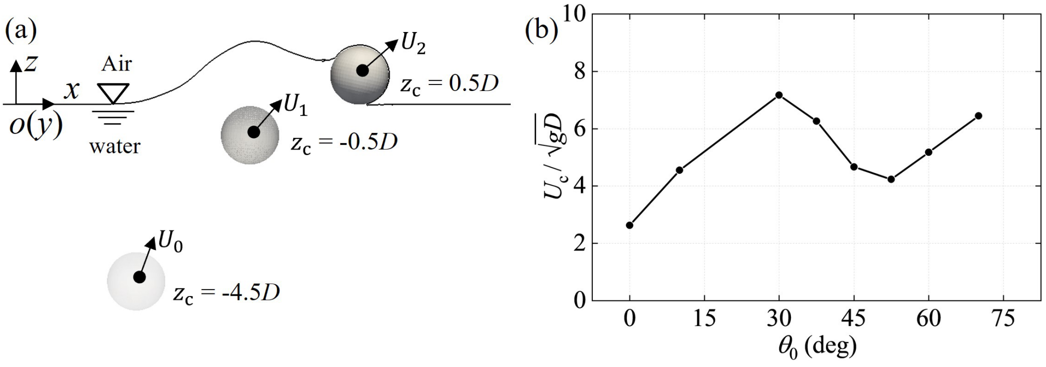

FIG. 4. (a) Schematic of the water exit configuration; (b) Variation of critical velocity with initial launch angle.

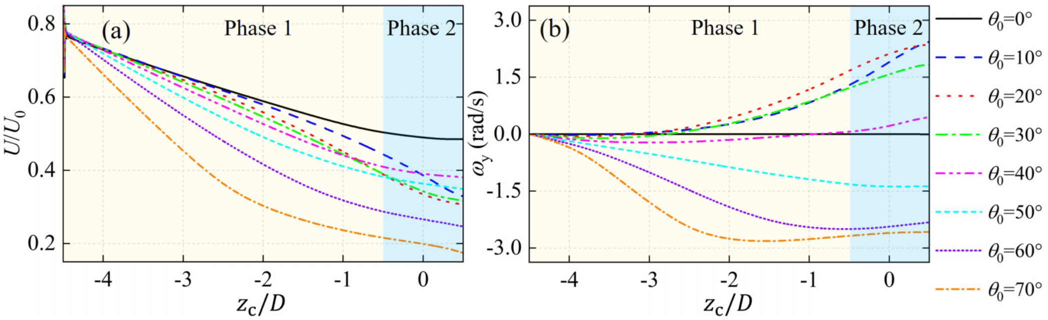

FIG. 5. Variation of (a) translational and (b) rotational velocities of the sphere with the vertical position of its center for different launch angles at $Fr = 8.6$.

the sphere is subjected to gravity, buoyancy, viscous drag, and wave-induced forces, which convert part of its kinetic energy into other forms, leading to a gradual velocity reduction. The critical velocity, U_c, is the minimum initial speed that allows the sphere to just exit the water (i.e., the highest position of its center is $z_c = 0.5D$). Figure 4(b) shows U_c as a function of θ_0. As expected, U_c is minimal at $\theta_0 = 0°$, where the sphere travels vertically upward and requires the least kinetic energy to emerge. Interestingly, U_c does not vary monotonically with θ_0. Instead, it first increases to a peak near $\theta_0 = 30°$, then decreases to a local minimum around $\theta_0 = 50°$, followed by a gradual increase.

To gain a more intuitive understanding of the velocity evolution during water exit, the translational velocity U and angular velocity ω_y of the sphere are plotted against the vertical position of its center for different launch angles, all at a fixed initial Froude number $Fr = 8.6$, as shown in Fig. 5. As indicated in Fig. 5(a), immediately after launch, the translational velocity undergoes a sharp reduction over a very short distance, reaching $U/U_0 \approx 0.78$. This initial drop is attributed to the transient added-mass effect [44], whereby the sphere must accelerate the surrounding quiescent water, effectively increasing its apparent inertia. Beyond this initial stage, U decreases gradually as the sphere ascends, reflecting the continuous conversion of kinetic energy into potential, viscous, and radiative energy. The rate of velocity reduction (i.e., the acceleration magnitude) in Phase 2 is smaller than that in Phase 1, indicating a slower deceleration once the sphere becomes partially emerged.

The rotational response is strongly dependent on the launch angle, as shown in Fig. 5(b). For $0° < \theta_0 < 40°$, ω_y remains positive throughout the motion, indicating clockwise rotation. For $40° < \theta_0 < 70°$, ω_y remains negative, corresponding to counterclockwise rotation. At $\theta_0 = 0°$, ω_y is nearly zero, implying negligible rotation, whereas at $\theta_0 = 40°$, ω_y changes sign from negative to positive, suggesting a transition from counterclockwise to clockwise rotation during ascent.

To further quantify velocity changes during the water-exit process, weanalyze velocity loss at different stages. Figure 6 presents the ratio of velocity loss to the initial velocity for various U_0 and θ_0 values. In Phase 1 (fully submerged), $(U_0 - U_1)/U_0$ decreases as U_0 increases, regardless of θ_0. This indicates that the relative velocity loss diminishes with higher U_0. In Phase 2 (partially submerged), $(U_1 - U_2)/U_0$ also decreases with increasing U_0, approaching a constant value dependent on θ_0. This suggests that the relative velocity loss while crossing the free surface tends to stabilize for large U_0, although the absolute energy dissipation still grows with U_0.

The influence of launch angle on velocity loss is further examined in Fig. 7 for $Fr = 8.6$. In Phase 1, $(U_0 - U_1)/U_0$ exhibits a non-monotonic variation with θ_0, reaching a local maximum at $\theta_0 = 20°$ and a local minimum at $\theta_0 = 45°$. Phase 2 shows a similar trend, with a local maximum at $\theta_0 = 10°$ and the same local minimum at $\theta_0 = 45°$. The total relative velocity loss, $(U_0 - U_2)/U_0$, obtained by summing the losses from both phases [Fig. 6(b)], increases and then decreases for $0° < \theta_0 < 45°$, reaching a local maximum at $\theta_0 = 15°$. Notably, the total loss at $\theta_0 = 45°$ is smaller than that at $\theta_0 = 10°$. For $\theta_0 > 45°$, the total relative loss increases steadily.

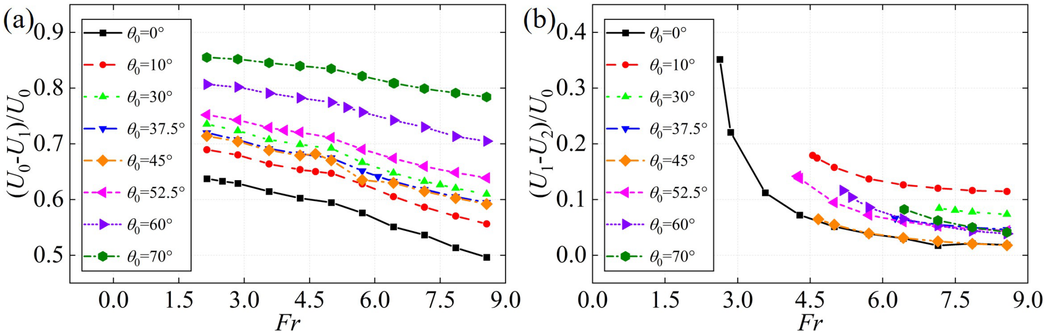

FIG. 6. Ratio of velocity loss to initial velocity in different stages of water exit: (a) Phase 1; (b) Phase 2.

The non-monotonic dependence of the velocity loss on the launch angle, as illustrated in Fig. 7(b), can be attributed to the combined effects of rotational dynamics and trajectory geometry. On one hand, the sphere's rotation itself varies non-monotonically with the initial angle, as discussed in Subsection V. C. The rotation enhances the energy loss during the oblique water-exit process through several coupled mechanisms. The induced surface-shear asymmetry promotes earlier flow separation and stronger vortex shedding, leading to increased viscous and turbulent dissipation. In addition, part of the translational kinetic energy is converted into rotational energy, which is subsequently dissipated by the surrounding viscous fluid. On the other hand, the trajectory length in Phase 1 increases with the launch angle, although trajectory deflection (addressed in Subsection V. D) should also be considered. A longer trajectory implies greater hydrodynamic work and, consequently, a larger energy dissipation, resulting in a higher velocity loss.

These combined mechanisms also account for the non-monotonic variation of the critical exit velocity with the launch angle, as shown in Fig. 4(b), since the critical exit velocity corresponds to the minimum attainable velocity loss during the water-exit process. Accordingly, Figs. 4(b) and 7(b) exhibit similar, though not identical, trends with respect to the launch angle. The similarity arises because both quantities are governed by the same underlying dissipative mechanisms associated with rotation-induced flow separation and trajectory-dependent hydrodynamic work. The slight discrepancy, however, stems from their different initial conditions: while the velocity loss reflects the actual kinetic energy dissipated for a given launch velocity ($Fr = 8.6$), the critical exit velocity represents the threshold at which the upward momentum just compensates the cumulative energy dissipation during the water exit.

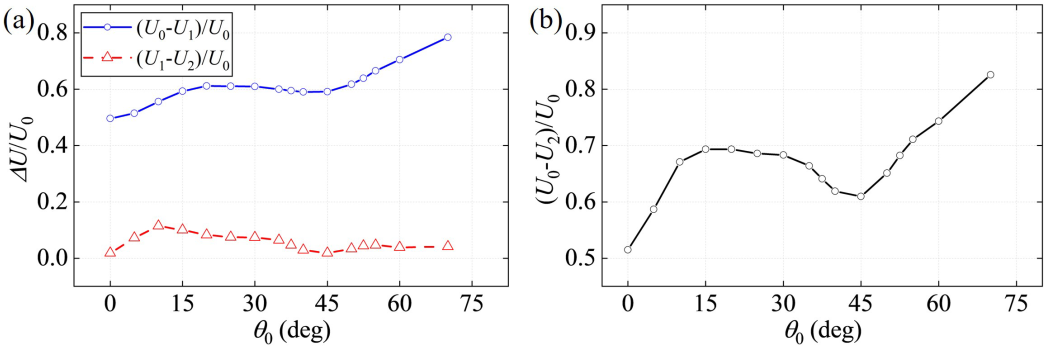

FIG. 7. Ratio of velocity loss to initial velocity for different launch angles at $Fr = 8.6$: (a) Phase 1 and Phase 2; (b) total loss.

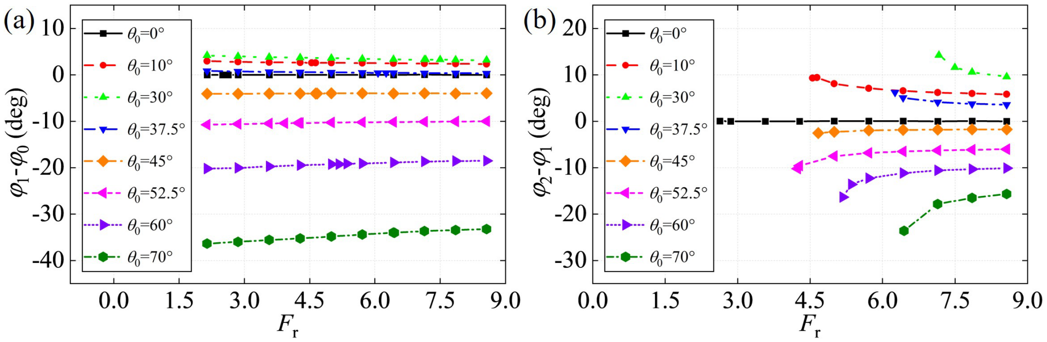

FIG. 8. Rotation angles in different stages of water exit as functions of initial velocity and launch angle: (a) Phase 1; (b) Phase 2.

C. Rotational dynamics

During the water exit process, the mutual action of gravity, buoyancy, drag, and wave-induced forces produces a net torque on the sphere, inducing rotational motion. Figure 8 shows the rotation angle φ at different stages for various initial velocities U_0 and launch angles θ_0. In Phase 1 (fully submerged), the incremental rotation $|\varphi_1 - \varphi_0|$ decreases slightly with increasing U_0, although the variation remains modest. For sufficiently large U_0, $\varphi_1 - \varphi_0$ approaches a constant value determined by θ_0. In Phase 2 (partially submerged), $|\varphi_2 - \varphi_1|$ decreases more significantly with U_0 and also tends toward a constant, again dependent on θ_0.

The sign of the incremental rotation indicates the rotation direction: a positive $\Delta\varphi$ ($\varphi_1 - \varphi_0$ or $\varphi_2 - \varphi_1$) corresponds to clockwise rotation, while a negative value indicates counterclockwise rotation. The sign $\Delta\varphi$ depends on θ_0. In both Phases, $\Delta\varphi$ is positive for $0^\circ < \theta_0 < 40^\circ$, indicating clockwise rotation, and negative for $\theta_0 > 40^\circ$, indicating counterclockwise rotation.

Figure 9 shows the dependence of rotation on θ_0 ($0^\circ < \theta_0 < 70^\circ$) for $Fr = 8.6$. In Phase 1 [Fig. 9(a)], $\varphi_1 - \varphi_0$ increases with θ_0 up to a maximum at $\theta_0 = 20^\circ$ (largest clockwise rotation), then decreases to a minimum at $\theta_0 = 70^\circ$ (largest counterclockwise rotation). At $\theta_0 = 0^\circ$ and 40°, $\varphi_1 - \varphi_0$ is close to zero, indicating negligible rotation. In Phase 2, $\varphi_2 - \varphi_1$ shows a similar non-monotonic trend, reaching a maximum at $\theta_0 = 20^\circ$, a minimum at $\theta_0 = 70^\circ$, and approaches zero at $\theta_0 = 0^\circ$ and 40°.

The total rotation over the entire water exit process, $\varphi_2 - \varphi_0$ [Fig. 8(b)], generally increases and then decreases with θ_0, peaking at $\theta_0 = 20^\circ$ (largest counterclockwise rotation) and reaching

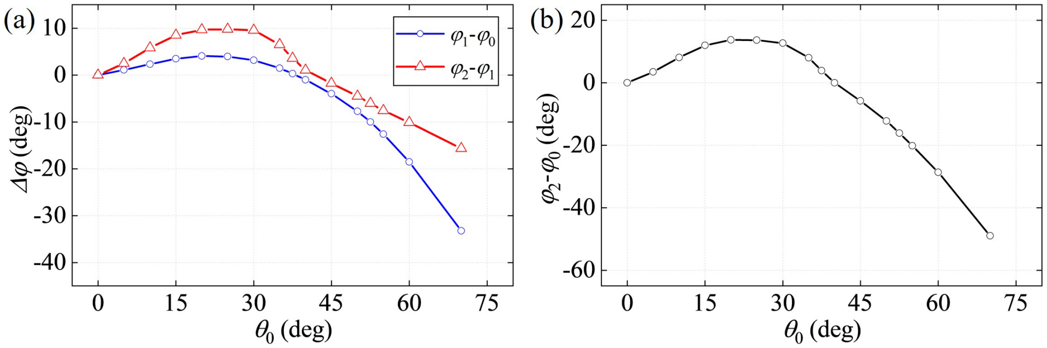

FIG. 9. Rotation angles at $Fr = 8.6$ for different launch angles: (a) Phase 1 and phase 2; (2) total rotation angle.

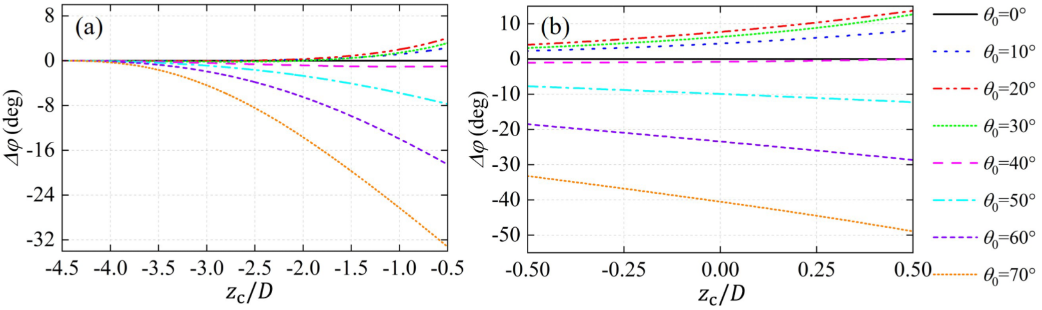

FIG. 10. Variation of rotation angle with the vertical position of the sphere's center at $Fr = 8.6$ for different launch angles: (a) Phase 1; (b) Phase 2.

a minimum at $\theta_0 = 70^\circ$ (largest clockwise rotation). At $\theta_0 = 0^\circ$ and 40°, the total rotation is negligible, indicating that the sphere maintains its orientation most effectively at these angles.

Although the total rotation of the sphere at $\theta_0 = 0^\circ$ and 40° is nearly zero in both cases, their underlying dynamics differ notably. At $\theta_0 = 0^\circ$, the sphere exhibits negligible angular velocity ($\omega_y \approx 0$), as shown in Fig. 5(b), and consequently its rotation angle remains almost unchanged ($\Delta\varphi \approx 0$). In contrast, at $\theta_0 = 40^\circ$, as shown in Fig. 10, $\Delta\varphi$ increases gradually during Phase 1 and then decreases during Phase 2, indicating that the sphere first rotates counterclockwise and subsequently reverses to clockwise rotation. This transition is consistent with the behavior of ω_y observed in Fig. 5(b).

D. Trajectory deflection during Phase 1

As shown in the preceding results, the sphere's rotation modifies the velocity vector and therefore inducing the trajectory deviation from a straight path. Figure 11 illustrates the trajectories at two launch angles, $\theta_0 = 30^\circ$ and $\theta_0 = 60^\circ$, for various initial velocities. In Phase 2 ($-0.5D < z_c < 0.5D$), the trajectory generally bends downward (clockwise) because the buoyancy force decreases as the sphere emerges, resulting in a net downward force that deflects the path. In contrast, the deflection direction in Phase 1 ($-4.5D < z_c <$-$0.5D$) depends on the launch angle: for $\theta_0 = 30^\circ$, the trajectory curves clockwise in phase, whereas in the same phase for $\theta_0 = 60^\circ$, it curves counterclockwise. The deflection direction is consistent with the sphere's rotation and is only weakly influenced by the initial velocity.

To assess the effect of launch angle, Fig. 12 shows the trajectories at $Fr = 8.6$ for $0^\circ < \theta_0 < 70^\circ$. With the exception for $\theta_0 = 0^\circ$ and 45°, where the trajectories remain nearly straight, all other

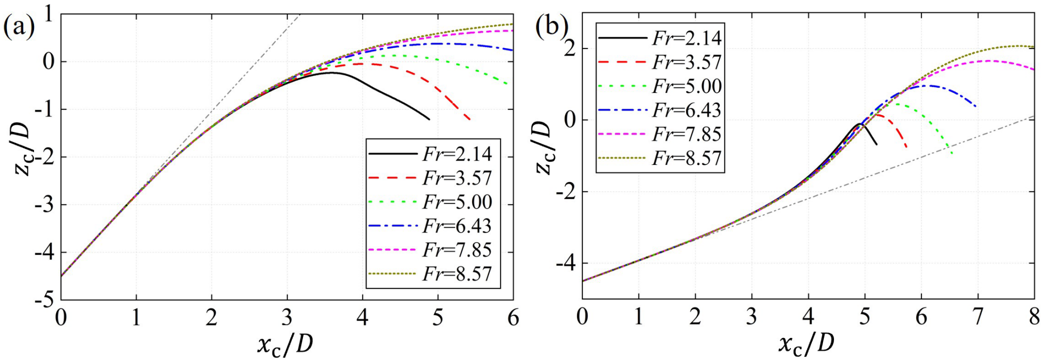

FIG. 11. Trajectories of the sphere for different initial velocities at (a) $\theta_0 = 30^\circ$ and (b) $\theta_0 = 60^\circ$.

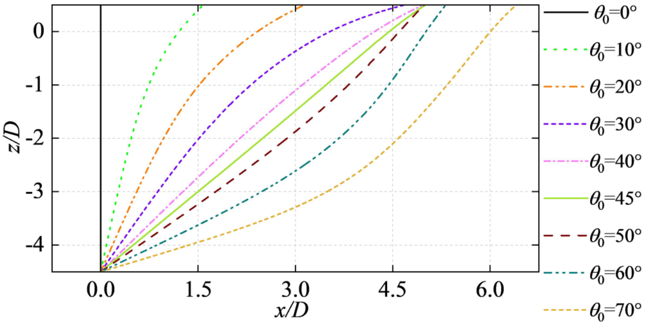

FIG. 12. Trajectories of the sphere at $Fr = 8.6$ for different launch angles.

launch angles produce noticeable deviations from the initial launch direction. The deflection direction is generally consistent with the sphere's rotation, being clockwise for $0^\circ < \theta_0 < 45^\circ$ and counterclockwise for $45^\circ < \theta_0 < 70^\circ$.

To quantify trajectory deflection, the lateral offset Δx is defined as the horizontal displacement of the sphere's center from the straight-line trajectory [Fig. 13(a)]:

$$\Delta x(z_c) = x_c - x_{\text{lin}}(z_c), \tag{10}$$

where

$$x_{\text{lin}}(z_c) = x_0 + \tan\theta(z_c - z_0), \tag{11}$$

and $(x_0,\ z_0)$ denotes the initial position of the sphere's center, while θ represents the instantaneous velocity angle at the initial point. Here, z_c is the instantaneous vertical coordinate of the sphere's center, and $x_{\text{lin}}(z_c)$ gives the corresponding horizontal coordinate assuming a straight-line motion.

Figure 13(b) presents the variation of Δx with the launch angle θ_0 at $Fr = 8.6$. The total trajectory deflection during the entire water-exit process is defined as $\Delta x(z_c = 0.5D)$, whereas the deflection during Phase 1 is given by $\Delta x(z_c = -0.5D)$. In both cases, the initial position is fixed at $(x_0,\ z_0) = (0D,\ -4.5D)$, and the initial velocity angle is $\theta = \theta_0$.

Notably, the starting point of Phase 2 corresponds to $z_c = -0.5D$, but the associated x-coordinate and velocity angle θ depend on both θ_0 and the initial velocity U_0. Consequently, $\theta \neq \theta_0$ at the beginning of Phase 2. Therefore, the difference $\Delta x(z_c = 0.5D) -\ \Delta x(z_c = -0.5D)$ does not represent the lateral offset accumulated during Phase 2.

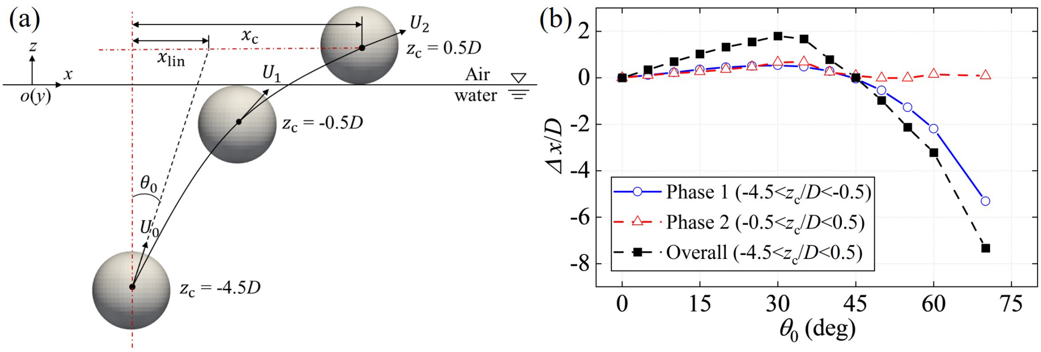

FIG. 13. (a) Schematic of the sphere's lateral offset; (b) Variation of lateral offset with initial launch angle at $Fr = 8.6$.

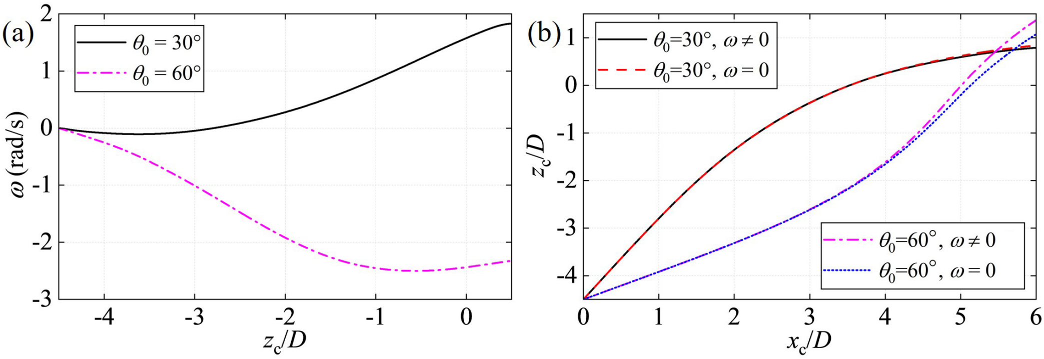

FIG. 14. (a) Variation of angular velocity (ω) about the y-axis with vertical position for $\theta_0 = 30°$ and 60° at $Fr = 8.6$; (b) comparison of trajectories with and without rotation for the same conditions.

For the overall trajectory ($-4.5 < z_c/D < 0.5$), the sphere deflects to the right ($\Delta x > 0$) when $0° < \theta_0 < 45°$, with a maximum offset occurring at $\theta_0 = 30°$. For $45° < \theta_0 < 70°$, the trajectory bends to the left ($\Delta x < 0$), reaching the largest deviation at $\theta_0 = 70°$.

During Phase 1 ($-4.5 < z_c/D < -0.5$), the trajectory exhibits a similar trend: it deflects to the right for $0° < \theta_0 < 45°$, with a maximum at $\theta_0 = 30°$. As θ_0 increases beyond 45°, the trajectory deflects gradually shifts leftward. The underlying mechanisms behind these deflection patterns are complex and are discussed in detail in Subsection V.E.

In Phase 2 ($-0.5 < z_c/D < 0.5$), the trajectory consistently deflects to the right for all launch angles, with the maximum deviation again occurring at $\theta_0 = 30°$. This rightward deflection primarily resulted from the reduction of buoyancy as the sphere emerges, which generates a net downward and rightward force on the body.

E. Underlying physics of trajectory deflection

The trajectory deflection observed during water exit is controlled primarily by the following factors: (i) the rotation of the sphere, (ii) the asymmetric distribution of wave-induced pressure on the sphere's surface, (iii) the image effect as the sphere approaches the free surface; and (iv) the interaction between the wake vortex and the free surface. Each mechanism isanalyzed in detail below.

1. Rotation effect

Due to the Magnus effect, sphere rotation alters the relative flow velocity on opposite sides of the body, producing a pressure difference that generates a lateral force perpendicular to the velocity vector and thus deflecting the trajectory.

Figure 14(a) shows the variation of the sphere's angular velocity about the y-axis, ω, with its vertical position during water exit at $Fr = 8.6$ for two initial launch angles, $\theta_0 = 30°$ and 60°. For $\theta_0 = 30°$, ω remains positive once $z_c/D >$-3, indicating clockwise rotation. The resulting lateral force deflects the trajectory to the right, consistent with the rotation direction. In contrast, for $\theta_0 = 60°$, ω remains negative, corresponding to counterclockwise rotation, which deflects the trajectory to the left.

To further assess the contribution of rotation to trajectory deflection, additional simulations were conducted at $Fr = 8.6$ in which the sphere's rotational degree of freedom about the y-axis was constrained, allowing only translational motion along the x- and z-axes. Two launch angles, $\theta_0 = 30°$ and 60°, were considered. Figure 14(b) compares the trajectories with and without rotation. The results show that rotation does not change the deflection direction but slightly increases its magnitude. For $\theta_0 = 30°$, the lateral offset $|\Delta x(z_c = 0.5D)|$ increases from $0.529D$ to $0.535D$, while for $\theta_0 = 60°$, it increases from $2.111D$ to $2.197D$.

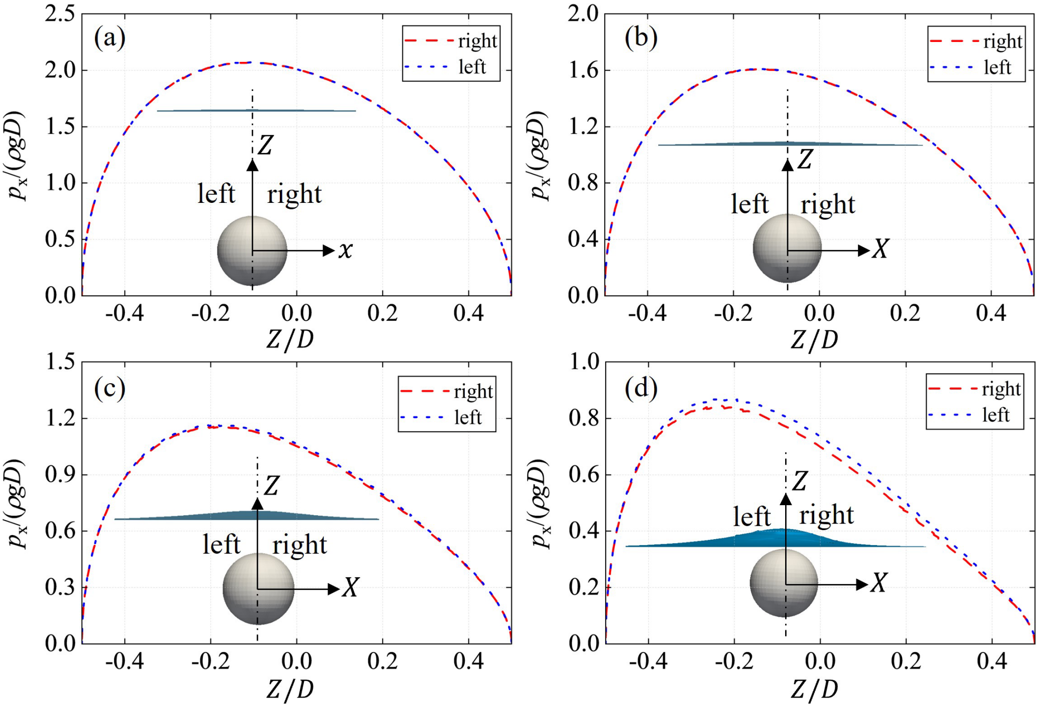

FIG. 15. Horizontal component of the hydrostatic pressure (p_x) on the sphere surface at different vertical positions for $Fr = 8.6$, $\theta_0 = 30^\circ$: (a) $z_c/D = -2.0$; (b) $z_c/D = -1.5$; (c) $z_c/D = -1.0$; (d) $z_c/D = -0.5$.

2. *Wave effect*

As the sphere emerges from the water, it induces nonlinear deformation of the free surface. This deformation results in local variations in surface elevation, which can be distributed asymmetrically in the horizontal direction relative to the sphere. Such asymmetry produces an imbalance in the horizontal component of the hydrostatic pressure on the two sides of the sphere, leading to trajectory deflection.

Figures 15 and 16 show the horizontal component of the surface pressure (p_x) on the left and right sides of the sphere for $Fr = 8.6$ and $\theta_0 = 30^\circ, 60^\circ$ at various vertical positions during emergence. The pressure imbalance becomes more pronounced as the sphere approaches the free surface, especially at $z_c/D = -0.5$. For $\theta_0 = 30^\circ$ (Fig. 15), the horizontal pressure component on the left side exceeds that on the right, producing a rightward (clockwise) trajectory deflection. In contrast, for $\theta_0 = 60^\circ$ (Fig. 16), the right-side component exceeds the left-side component, resulting in a leftward (counterclockwise) deflection.

It is worth noting that the magnitude difference in the horizontal hydrostatic pressure between the two sides is relatively small. Therefore, the contribution of wave-induced hydrostatic pressure imbalance to trajectory deflection during water exit is small.

3. *Image effect*

The influence of the free surface on the sphere trajectory can be interpreted through an image-dipole model [45,46]. As illustrated in Fig. 17, consider a neutrally buoyant sphere moving in the x-z plane with instantaneous velocity

$$\boldsymbol{U}(t) = (U_x(t), U_z(t)) = U(t)(\sin\theta(t),\ \cos\theta(t)), \tag{12}$$

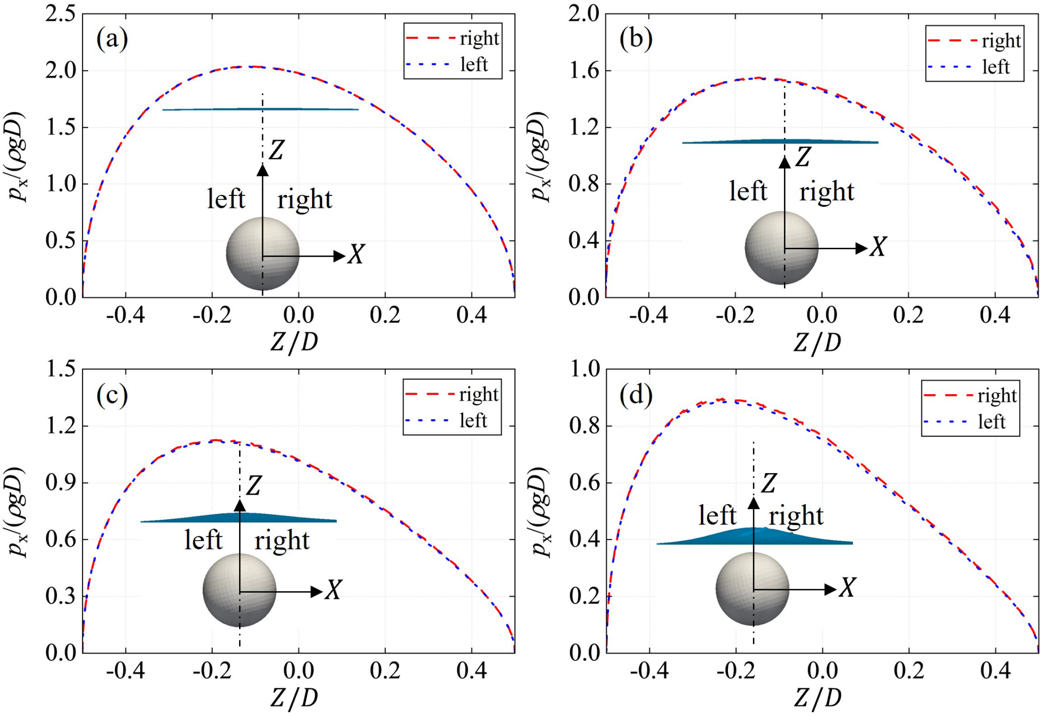

FIG. 16. Horizontal component of the hydrostatic pressure (p_x) on the sphere surface at different vertical positions for $Fr = 8.6$, $\theta_0 = 60^\circ$: (a) $z_c/D = -2.0$; (b) $z_c/D = -1.5$; (c) $z_c/D = -1.0$; (d) $z_c/D = -0.5$.

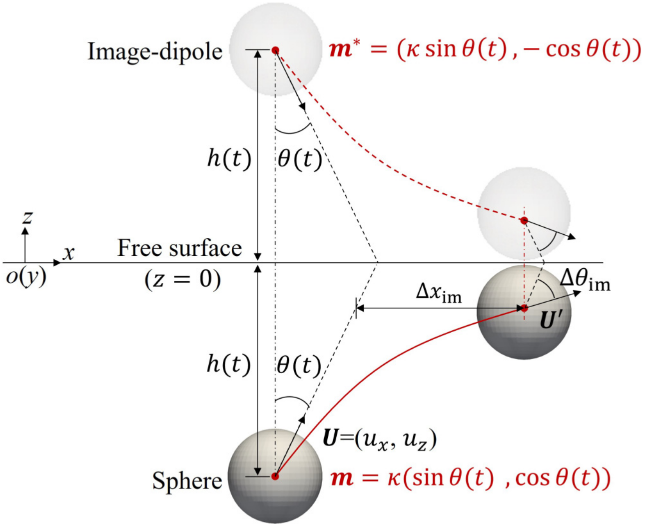

FIG. 17. A schematic of the image-dipole configuration.

where $\theta(t)$ denotes the instantaneous trajectory angle (measured from the positive z-axis toward the x-axis). The initial condition is given by the launch angle $\theta_0 = \theta(t_0)$.

In potential flow, the near-field disturbance of the sphere is approximated by a three-dimensional dipole with moment

$$\boldsymbol{m} = \kappa(\sin\theta(t), \cos\theta(t)), \tag{13}$$

where $\kappa > 0$ is the dipole strength. For a rigid sphere of radius a translating in an unbounded fluid, the classical potential-flow solution gives $\kappa = \frac{1}{2}a^3U(t)$. To account for finite-depth and unsteady effects near free surface, we adopt the generalized form

$$\kappa = Ca^3U(t), \tag{14}$$

where C is an order-one dimensionless coefficient. In the ideal unbounded case, $C = 0.5$. Near the free surface, however, surface proximity, unsteadiness, and wake interactions modify the effective dipole strength. Numerical and experimental evidence indicates that C remains of order unity, typically within 0.4–1.0 [47], so it should be regarded as an effective coefficient rather than a fixed constant.

To satisfy the boundary condition at the free surface ($z = 0$), the method of images is applied. Under a Neumann-type (slip) condition, the normal component of the dipole orientation is reversed while the tangential component is preserved, giving

$$\boldsymbol{m}^* = (\kappa\sin\theta(t), -\kappa\cos\theta(t)). \tag{15}$$

The velocity induced by a dipole $\boldsymbol{m}$ at position $\boldsymbol{r}$ is

$$\boldsymbol{u}(\boldsymbol{r}) = \frac{1}{4\pi}\left[\frac{3\boldsymbol{r}(\boldsymbol{m}\cdot\boldsymbol{r})}{|\boldsymbol{r}|^5} - \frac{\boldsymbol{m}}{|\boldsymbol{r}|^3}\right]. \tag{16}$$

Evaluating the contribution of the image dipole at the sphere center, separated vertically by $2h$, gives

$$u_x = -\frac{\kappa}{32\pi h^3}\sin\theta(t), \quad u_z = -\frac{\kappa}{16\pi h^3}\cos\theta(t), \tag{17}$$

where $h = h(t)$ is the instantaneous distance from the sphere center to the free surface.

The incremental change in the trajectory angle $\theta(t)$ is determined by the rotation of the velocity vector. For a small perturbation $\boldsymbol{u}$, the signed angular change is

$$\delta\theta(t) = \frac{\hat{\boldsymbol{y}}\cdot(\boldsymbol{U}\times\boldsymbol{u})}{|\boldsymbol{U}|^2} = \frac{U_zu_x - U_xu_z}{U_x{}^2 + U_z{}^2}, \tag{18}$$

where $\hat{\boldsymbol{y}}$ is the out-of-plane unit vector. Substituting $\boldsymbol{U}(t)$ and Eq. (17) into Eq. (18) yields

$$\delta\theta(h,\theta) = \frac{C}{64\pi}\left(\frac{a}{h}\right)^3\sin 2\theta(t). \tag{19}$$

Notably, the dependence on U cancels because the induced velocity scales with $\kappa \propto U$ while Eq. (18) normalizes by $|\boldsymbol{U}|^2$. As a result, the image-induced turning tendency depends only on the geometry (a/h) and the instantaneous angle $\theta(t)$, but not on the speed magnitude.

Equation (19) shows that the instantaneous turning tendency induced by the image effect is always positive for $0^\circ < \theta(t) < 90^\circ$, indicating a clockwise deflection. The effect vanishes for vertical ($\theta = 0^\circ$) and horizontal ($\theta = 90^\circ$) orientations and reaches its maximum near $\theta = 45^\circ$. The factor $(a/h)^3$ indicates that the contribution is strongly localized when the sphere center is within a few radii below the free surface.

In principle, the cumulative deflection angle due to the image effect should be obtained by integrating Eq. (19) over the exit process with the full-time histories $h(t)$ and $\theta(t)$:

$$\Delta\theta_{\text{im}} = \int_{t_0}^{t_1}\delta\theta(h(t),\theta(t))dt, \tag{20}$$

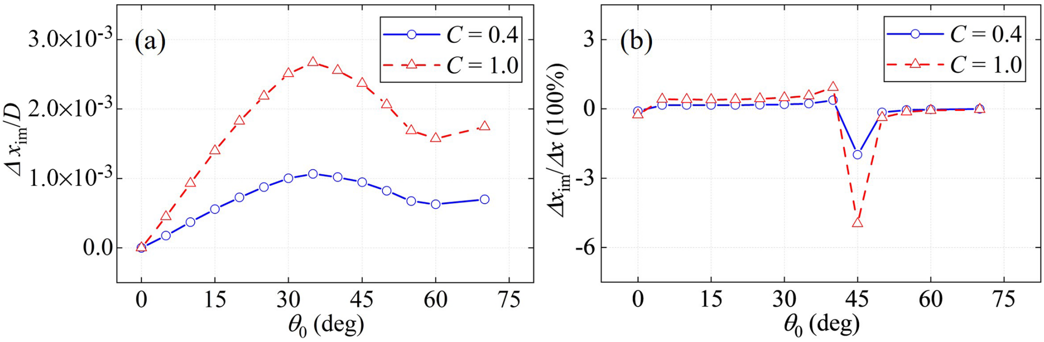

FIG. 18. Variation of lateral offset indued by the image effect with initial launch angle at $Fr = 8.6$: (a) absolute displacement; (b) relative magnitude compared with the trajectory deflection in Phase 1.

where t_0 denotes the initial launch time and t_1 the instant when the sphere reaches the free surface (i.e., $z_c = -0.5D$).

A rigorous first-order expression for the image-induced lateral offset can be derived directly from the kinematics. The horizontal displacement of the sphere due to the image effect, evaluated at the emergence instant, is

$$\Delta x_{\mathrm{im}} = \int_{t_0}^{t_1} u_x dt - \tan\theta(t_1) \int_{t_0}^{t_1} u_z dt = \int_{z_0}^{z_1} \frac{U_z u_x - U_x u_z}{U_z{}^2} dz, \tag{21}$$

where $z_0 = -4.5D$ and $z_1 = -0.5D$ correspond to the vertical positions of the sphere center at t_0 and t_1, respectively.

Substituting Eqs. (14) and (17) into Eq. (21) gives a compact first-order expression for the lateral offset:

$$\Delta x_{\mathrm{im}} = \frac{Ca^3}{32\pi} \int_{z_0}^{z_1} \frac{\tan\theta(z)}{h(z)^3} dz, \tag{22}$$

which explicitly accounts for the instantaneous variation of the trajectory angle $\theta(z)$ and immersion depth $h(z)$ throughout the exit process.

According to Eq. (22), the lateral displacement induced by the image effect, Δx_{im}, can be evaluated using the time histories of the instantaneous velocities and sphere position during the water-exit process. As shown in Fig. 18(a), Δx_{im} remains positive for all cases, indicating that the image effect consistently deflects the trajectory to the right (clockwise). Nevertheless, regardless of whether the dipole-strength coefficient C is 0.4 or 1.0, Δx_{im} is always smaller than $0.003D$, implying that the image effect contributes only a minor portion to the overall trajectory deviation.

Figure 18(b) further compares the image-induced and total lateral displacements during Phase 1 through the ratio $\Delta x_{\mathrm{im}}/\Delta x$. The ratio remains within [−2%, 6%] across all launch angles and reaches its maximum at $\theta_0 = 45^\circ$, primarily because the total deflection Δx is smallest at this angle. These results demonstrate that the image effect acts as a secondary mechanism governing the trajectory deflection of the sphere during Phase 1 of the water-exit process.

4. Wake effect

During water exit, the sphere sheds vortices whose evolution becomes asymmetric in the vicinity of the interface. Prior studies (e.g., Ohring and Lugt [48]) demonstrated that vortex rings approaching a free surface interact strongly with it and that the interaction depends sensitively on the incidence angle. Such interactions modify the surrounding flow and can lead to either clockwise or counterclockwise trajectory deflection.

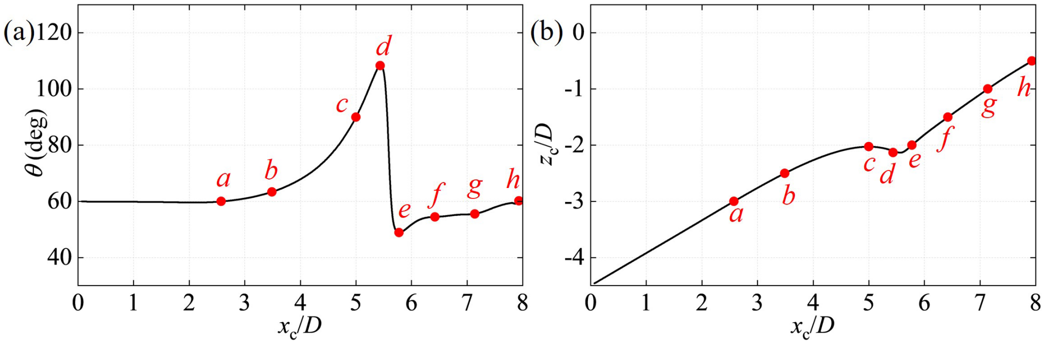

FIG. 19. Sphere dynamics in the baseline case at different vertical positions (*a*: $z_c/D = -3.0$; *b*: $z_c/D = -2.5$; *c*: $z_c/D = -2.03$; *d*: $z_c/D = -2.13$; *e*: $z_c/D = -2.0$; *f*: $z_c/D = -1.5$; *g*: $z_c/D = -1.0$; *h*: $z_c/D = -0.5$): (a) velocity direction; (b) trajectory.

To isolate the hydrodynamic contribution of the wake-interface interaction while excluding rotation and wave-induced pressure, a baseline simulation was performed using only the underwater portion of the domain (see Fig. 2). The free surface was replaced by a shear-free, impermeable lid enforcing zero normal velocity ($\boldsymbol{u} \cdot \boldsymbol{n} = 0$) and zero tangential shear ($\tau_t = 0$), and the sphere rotation was suppressed; all other conditions were identical. In what follows, this idealized boundary is referred to as the lid. The baseline case corresponds to a launch angle $\theta_0 = 60^\circ$ and $Fr = 8.6$.

Figure 19 illustrates the evolution of the motion direction and trajectory in the baseline case. During the initial stage ($-4.5 < z_c/D < -3$), the trajectory remains aligned with the launch direction. As the sphere rises to $-3 < z_c/D < -2.03$, the wake loses its symmetry due to the presence of the lid [Fig. 20(c)]. The upper-left vortex is lifted toward the narrow gap between the sphere and the lid. The induced velocity field produces local deceleration above the sphere apex, forming a

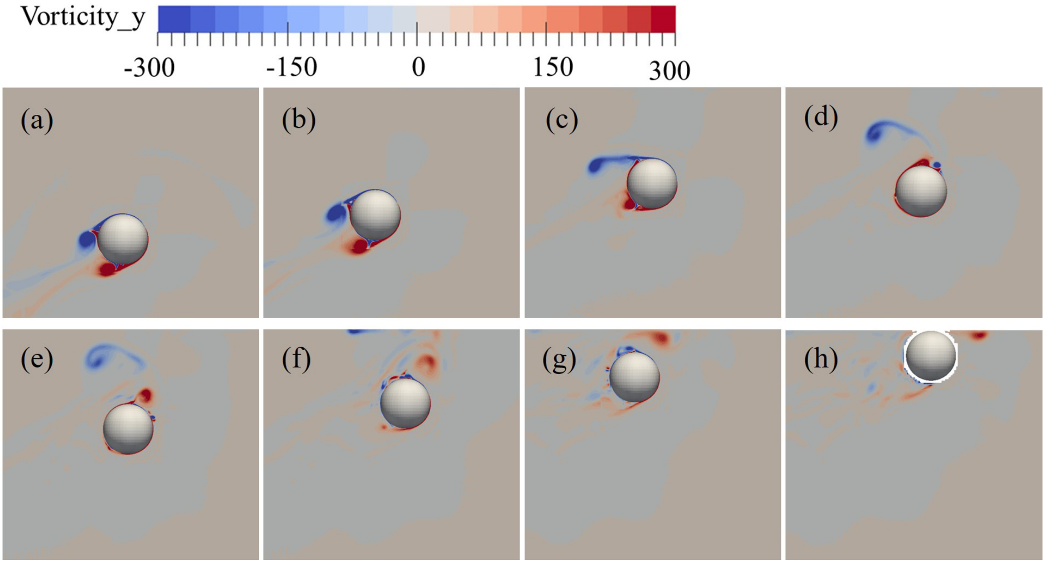

FIG. 20. Vortex structures in the baseline case at different vertical positions: (a) $z_c/D = -3.0$; (b) $z_c/D = -2.5$; (c) $z_c/D = -2.03$; (d) $z_c/D = -2.13$; (e) $z_c/D = -2.0$; (f) $z_c/D = -1.5$; (g) $z_c/D = -1.0$; (h) $z_c/D = -0.5$.

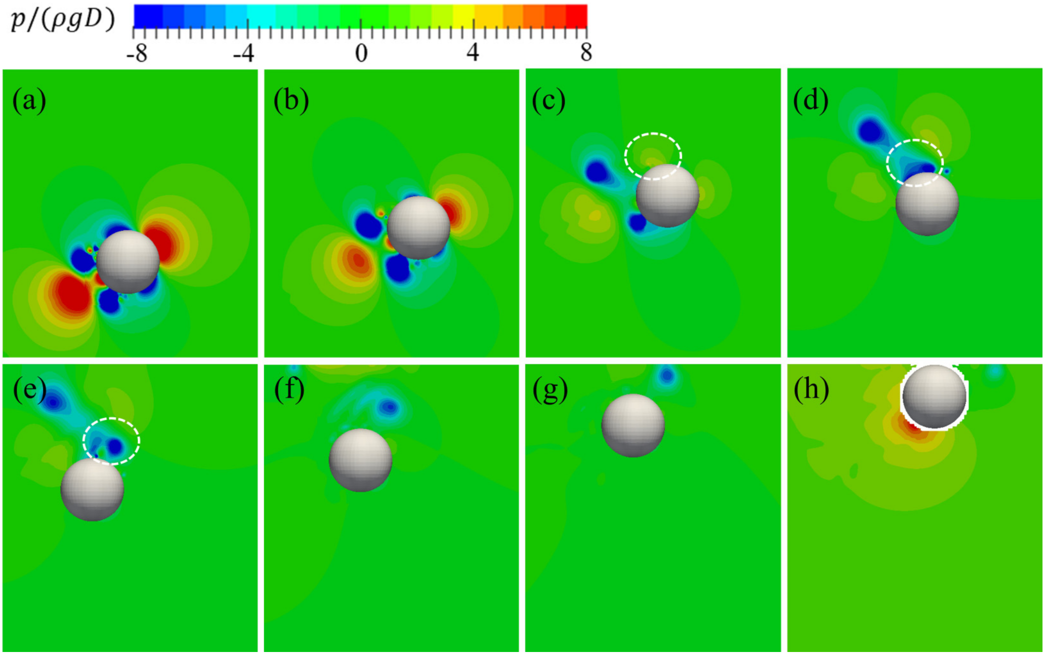

FIG. 21. Pressure distribution in the baseline case at different vertical positions: (a) $z_c/D = -3$; (b) $z_c/D = -2.5$; (c) $z_c/D = -2.03$; (d) $z_c/D = -2.13$; (e) $z_c/D = -2.0$; (f) $z_c/D = -1.5$; (g) $z_c/D = -1.0$; (h) $z_c/D = -0.5$.

near-stagnation zone and hence a high-pressure patch on the upper surface [Fig. 21(c), white dashed line]. The trajectory deflects clockwise, and the velocity angle θ reaches a maximum of 108° at $z_c/D = -2.13$.

As the shed vortex convects further and passes over the sphere, it is redirected along the lid by the shear-free condition. The associated induced motion causes tangential acceleration across the apex, giving rise to a low-pressure region above the sphere [Figs. 21(d) and 21(e)]. The transition from high to low pressure correlates with the migration of the vortex from a lateral to an overhead position. A rapid counterclockwise correction of the trajectory follows, with θ decreasing to 54° at $z_c/D = -2$. Thereafter, θ gradually increases again, indicating a mild clockwise drift, consistent with an image-effect contribution that intensifies as the interface is approached.

Notably, the baseline trajectory in Fig. 19(b) differs substantially from that obtained with a deformable free surface under identical initial conditions [Fig. 11(b), solid green line]. Such a discrepancy is expected, because the interaction between the shed vortex and the top boundary is strongly influenced by surface deformation and wave radiation. These processes, which facilitate momentum exchange and feedback between the wake and the free surface, are artificially suppressed when the top boundary is treated as rigid [49,50]. Similar sensitivities have been widely reported for near-surface spheres, where the proximity to a moving interface modifies vortex shedding patterns and hydrodynamic loads [47,51]. The underlying mechanism can be attributed to the radiation of gravity-capillary waves induced by vortical motion, which in turn alters the local pressure field and vortex evolution [52,53].

To visualize these differences under otherwise identical conditions ($\theta_0 = 60°$, $Fr = 8.6$), Fig. 22 presents the evolving vortex structures for the free-surface case at successive vertical positions. The white arrows indicate the instantaneous velocity direction of the sphere, from which the symmetry of the wake vorticity can be assessed. When the shear-free lid is replaced by a moving free surface, the shed vortex no longer passes distinctly over the sphere apex. Instead, the deformable interface modifies the wake evolution through wave radiation and vortex-interface coupling, which alters the

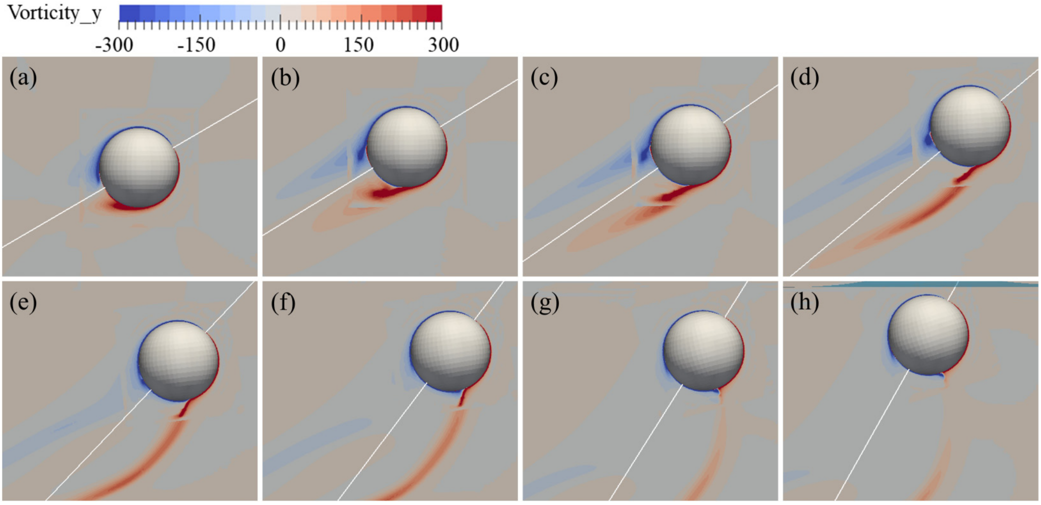

FIG. 22. Vortex structures in the free surface case ($\theta_0 = 60^\circ$, $Fr = 8.6$) at different vertical positions: (a) $z_c/D = -4.0$; (b) $z_c/D = -3.5$; (c) $z_c/D = -3.0$; (d) $z_c/D = -2.5$; (e) $z_c/D = -2.0$; (f) $z_c/D = -1.5$; (g) $z_c/D = -1.0$; (h) $z_c/D = -0.5$.

trajectory and strength of the shed vortex in the near wake. The resulting wake asymmetry generates a time-dependent pressure imbalance on the sphere surface, leading to the observed variations in the transverse force (F_v) and pitching moment (M_y), as presented in Fig. 23(a).

To further verify that the wake-surface interaction is the primary cause of trajectory bending, an inviscid simulation was conducted under identical initial conditions, in which fluid viscosity was neglected, and the boundary condition on sphere surface was treated as slip. This configuration effectively suppresses the wake vorticity while retaining the effects of free surface wave radiation and added mass dynamics. As shown in Fig. 23(b), once the wake vorticity is eliminated, the trajectory bending is also markedly reduced, confirming that the interaction between the free surface and the vorticity wake is the dominant mechanism responsible for the trajectory deflection.

From the above analysis, it can be concluded that the trajectory deflection of the sphere during Phase 1 is primarily governed by the wake effect, whereas the image effect serves as a secondary mechanism, contributing no more than about 6% to the total deviation. The influences of the wave effect and rotation effect are comparatively minor.

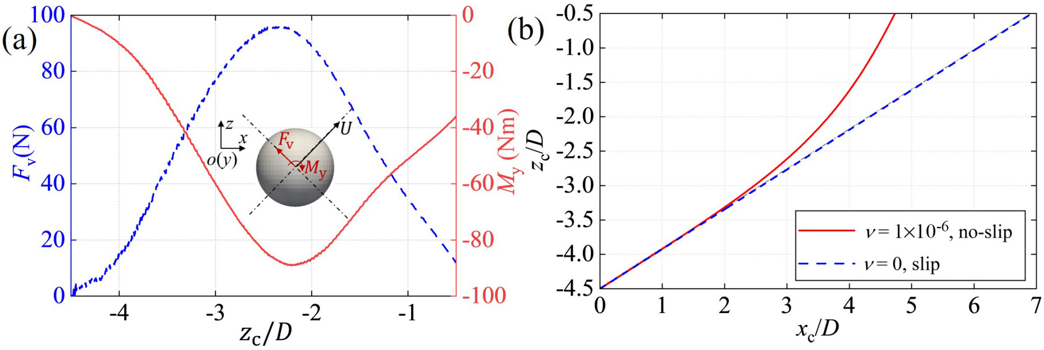

FIG. 23. (a) Transverse force F_v and pitching moment M_y acting on the sphere in the free surface case; (b) Comparison of trajectories between the free surface ($\nu = 1 \times 10^{-6}$, no-slip) and inviscid ($\nu = 0$, slip) cases at $\theta_0 = 60^\circ$ and $Fr = 8.6$.

VI. CONCLUSIONS

In this study, a CFD framework combining Large-Eddy Simulation with the overset mesh technique has been employed to investigate the water exit dynamics of a neutrally buoyant sphere. The sphere is launched from a fixed submergence depth with varying initial velocities and launch angles. The simulations resolve the sphere's velocity, rotation, and trajectory, and provide physical insight into the underlying mechanisms. Particular attention is given to the influence of the initial velocity (U_0) and launch angle (θ_0) on the kinematics during water exit.

The water exit motion is divided into two stages. In Phase 1 (fully submerged, $z_c < -0.5D$), the critical velocity U_1 exhibits a nonlinear dependence on θ_0: it increases, then decreases, and rises again, reaching a local maximum at $\theta_0 = 30^\circ$ and a minimum at $\theta_0 = 52.5^\circ$, with values at $\theta_0 = 10^\circ$ and 52.5° being nearly identical. The velocity loss ratio $(U_0 - U_1)/U_0$ decreases as U_0 increases, regardless of θ_0. In Phase 2 (partially submerged, $-0.5D < z_c < 0.5D$), the velocity loss ratio $(U_1 - U_2)/U_0$ approaches a constant as U_0 increases, with the constant determined by θ_0. The overall velocity reduction $(U_0 - U_2)/U_0$ shows a non-monotonic trend with θ_0, peaking at 15° and reaching a minimum at 45°, with values at $\theta_0 = 10^\circ$ and 52.5° again being nearly equal.

The sphere undergoes rotation during exit. The incremental rotation angle in both phases, $\varphi_1 - \varphi_0$ and $\varphi_2 - \varphi_1$, decreases with increasing U_0 and converges to a θ_0-dependent constant. The rotation direction is also strongly linked to θ_0: negligible rotation occurs at $\theta_0 = 0^\circ$ and 40°; clockwise rotation appears when $0^\circ < \theta_0 < 40^\circ$; and counterclockwise rotation occurs when $40^\circ < \theta_0 < 70^\circ$. The total rotation $\varphi_2 - \varphi_0$ varies nonlinearly with θ_0, generally increasing and then decreasing, with a maximum counterclockwise rotation at $\theta_0 = 20^\circ$ and the largest clockwise rotation at $\theta_0 = 70^\circ$.

The overall trajectory deflects laterally in most cases, except at $\theta_0 = 0^\circ$ and 45°. The deflection direction is independent of U_0 but strongly dependent on θ_0: it is clockwise for $0^\circ < \theta_0 < 45^\circ$, with the maximum offset at $\theta_0 = 30^\circ$, and counterclockwise for $45^\circ < \theta_0 < 70^\circ$, with increasing magnitude as θ_0 increases. In Phase 1, the trajectory exhibits the same angular dependence, bending downward (clockwise) for $0^\circ < \theta_0 < 45^\circ$ with the largest deviation at $\theta_0 = 30^\circ$, and upward (counterclockwise) for $45^\circ < \theta_0 < 70^\circ$ with increasing magnitude. The dominant mechanisms are the interaction between the shed vortices and the free surface and the image effect, whose combined action dictates the deflection direction. Secondary effects, including the sphere's own rotation and asymmetric wave-induced pressure distribution, further amplify the trajectory deviation without altering its direction. In Phase 2, the trajectory shows a consistent downward (clockwise) bending, primarily due to the reduction of buoyancy as the sphere emerges.

This study enhances the understanding of velocity loss, rotational dynamics, and trajectory deflection during water exit, highlighting the critical roles of launch velocity and angle. These findings are relevant for the design of underwater vehicles, projectiles, and marine structures where accurate motion and stability predictions are required. Nevertheless, the present analysis does not account for factors such as initial submergence depth and body geometry, which are also expected to significantly affect the dynamics. Future research should address these aspects to develop a more comprehensive picture of water exit processes.

ACKNOWLEDGMENTS

The authors gratefully acknowledge the support of the EPSRC High-End Computing Consortium for Wave Structure Interaction (HEC-WSI), under Grant No. EP/X035751/1, for providing access to ARCHER2 HPC resources.

DATA AVAILABILITY

The data that support the findings of this article are not publicly available. The data are available from the authors upon reasonable request.

[1] X. Sun, J. Cao, Y. Li *et al.*, Efficient prediction method for the water-exit characteristics of unmanned aerial–underwater vehicles, Ocean Eng. **302**, 117403 (2024).

[2] B. Liu, X. Chen, E. Li *et al.*, Numerical analysis on water-exit process of submersible aerial vehicle under different launch conditions, J. Mar. Sci. Eng. **11**, 839 (2023).

[3] X. Huang, Y. Dai, and X. Zhu, Numerical study of vehicle motion during water exit under combined lifting force and wave action, Phys. Fluids **36**, 107144 (2024).

[4] X. Huang, Y. Dai, C. Liu *et al.*, Water-exit impact of deep-sea mining vehicles: Experimental and numerical investigations, Ocean Eng. **302**, 117444 (2024).

[5] V. Saro-Cortes, Y. Cui, T. Dufficy, A. Boctor, B. E. Flammang, and A. Wissa, An adaptable flying fish robotic model for aero-and hydrodynamic experimentation, Integr. Comp. Biol. **62**, 1202 (2022).

[6] A. Khosronejad, L. Mendelson, A. H. Techet *et al.*, Water exit dynamics of jumping archer fish: Integrating two-phase flow large-eddy simulation with experimental measurements, Phys. Fluids **32**, 011904 (2020).

[7] A. A. Korobkin, T. I. Khabakhpasheva, and K. J. Maki, Hydrodynamic forces in water exit problems, J. Fluids Struct. **69**, 16 (2017).

[8] T. T. Truscott, B. P. Epps, and R. H. Munns, Water exit dynamics of buoyant spheres, Phys. Rev. Fluids **1**, 074501 (2016).

[9] H. Zheng, H. Qiang, Y. Zhu *et al.*, Overview of theory, simulation, and experiment of the water exit problem, J. Mar. Sci. Eng. **12**, 1764 (2024).

[10] B. Y. Ni, A. M. Zhang, and G. X. Wu, Simulation of complete water exit of a fully-submerged body, J. Fluids Struct. **58**, 79 (2015).

[11] K. Takamure and T. Uchiyama, Energy transition in air of a sphere launched vertically upward in water, Ocean Eng. **207**, 107426 (2020).

[12] Q. G. Wu, B. Y. Ni, and X. L. Bai *et al.*, Experimental study on large deformation of free surface during water exit of a sphere, Ocean Eng. **140**, 369 (2017).

[13] G. Colicchio, M. Greco, M. Miozzi *et al.*, Experimental and numerical investigation of the water-entry and water-exit of a circular cylinder, in *Proceedings of the 24th International Workshop on Water Waves and Floating Bodies* (Zelenogorsk, Russian Federation, 2009), pp. 19–22.

[14] H. Yun, Q. Liu, Z. Zeng, and L. Lian, Experimental study on water-exit of cylinder, Ocean Eng. **293**, 116585 (2024).

[15] G. Fu, J. Zhao, L. Sun, and Y. Lu, Experimental investigation of the characteristics of an artificial cavity during the water-exit of a slender body, J. Mar. Sci. Appl. **17**, 578 (2018).

[16] K. Takamure and T. Uchiyama, Effect of density of a sphere launched vertically in water on the water-surface behavior and sphere motion in air, Phys. Fluids **32**, 113313 (2020).

[17] K. Takamure and T. Uchiyama, Dynamics of a sphere launched vertically in water, Powder Technol. **372**, 246 (2020).

[18] H. Haohao, S. Yanping, Y. Jianyang *et al.*, Numerical analysis of water exit for a sphere with constant velocity using the lattice Boltzmann method, Appl. Ocean Res. **84**, 163 (2019).

[19] X. Zhu, O. M. Faltinsen, and C. Hu, Water entry and exit of a horizontal circular cylinder, J. Offshore Mech. Arct. Eng. **129**, 253 (2007).

[20] G. Zhang, C. You, H. Wei *et al.*, Experimental study on the effects of brash ice on the water-exit dynamics of an underwater vehicle, Appl. Ocean Res. **117**, 102948 (2021).

[21] C. You, T. Sun, G. Zhang *et al.*, Numerical study on effect of brash ice on water exit dynamics of ventilated cavitation cylinder, Ocean Eng. **245**, 110443 (2022).

[22] H. Wang, Z. Huang, and Z. Guo, Numerical study on the influence of floating ice on the water-exit hydrodynamic characteristics of a trans-media vehicle, J. Phys.: Conf. Ser. **2478**, 112008 (2023).

[23] V. T. Nguyen, T. H. Phan, and T. N. Duy *et al.*, Unsteady cavitation around submerged and water-exit projectiles under the effect of the free surface: A numerical study, Ocean Eng. **263**, 112368 (2022).

[24] P. Lin, A fixed-grid model for simulation of a moving body in free surface flows, Comput. Fluids **36**, 549 (2007).

[25] C. Zhang, W. Zhang, N. Lin *et al.*, A two-phase flow model coupling with volume of fluid and immersed boundary methods for free surface and moving structure problems, Ocean Eng. **74**, 107 (2013).

[26] V. B. Nguyen, Q. V. Do, and V. S. Pham, An OpenFOAM solver for multiphase and turbulent flow, Phys. Fluids **32**, 043303 (2020).

[27] Y. Chen, Z. Gong, J. Li *et al.*, Numerical investigation on the regime of cavitation shedding and collapse during the water-exit of submerged projectile, J. Fluids Eng. **142**, 011403 (2020).

[28] X. Zhang, X. Lyu, and X. Fan, Numerical study on the vertical water exit of a cylinder with cavity, China Ocean Engineering **36**, 734 (2022).

[29] Z. Qu, J. Cui, X. Chen *et al.*, Study on vortex structure and hydrodynamic characteristics of water-exit projectile with shoulder ventilation, Ocean Eng. **313**, 119622 (2024).

[30] Q. S. Zhang, F. R. Ming, C. Liu *et al.*, Experimental study of the effect of the ventilation mode on the water-exit of the vehicle, Phys. Fluids **36**, 082108 (2024).

[31] C. Guo, T. Liu, H. Hao *et al.*, Evolution of water column pulled by partially submerged spheres with different velocities and submergence depths, Ocean Eng. **187**, 106087 (2019).

[32] Y. Huang, Q. Xiao, and Q. Zhu, Dynamics and energetics of a sphere during water exit, Phys. Fluids **37**, 023323 (2025).

[33] J. Smagorinsky, General circulation experiments with the primitive equations: I. The basic experiment, Mon. Weather Rev. **91**, 99 (1963).

[34] C. W. Hirt and B. D. Nichols, Volume of fluid (VOF) method for the dynamics of free boundaries, J. Comput. Phys. **39**, 201 (1981).

[35] S. T. Miller, R. L. Campbell, C. W. Elsworth, J. S. Pitt, and D. A. Boger, An overset grid method for fluid-structure interaction, World J. Mech. **4**, 217 (2014).

[36] R. I. Issa, Solution of the implicitly discretised fluid flow equations by operator-splitting, J. Comput. Phys. **62**, 40 (1986).

[37] S. V. Patankar and D. B. Spalding, A calculation procedure for heat, mass and momentum transfer in three-dimensional parabolic flows[M]//Numerical prediction of flow, heat transfer, turbulence and combustion. Pergamon, 54–73 (1983).

[38] S. M. Damián and N. M. Nigro, An extended mixture model for the simultaneous treatment of small-scale and large-scale interfaces, Int. J. Numer. Methods Fluids **75**, 547 (2014).

[39] M. Rudman, Volume-tracking methods for interfacial flow calculations, Int. J. Numer. Methods Fluids **24**, 671 (1997).

[40] S. T. Zalesak, Fully multidimensional flux-corrected transport algorithms for fluids, J. Comput. Phys. **31**, 335 (1979).

[41] U. Piomelli and E. Balaras, Wall-layer models for large-eddy simulations, Annu Rev Fluid Mech **34**, 349 (2002).

[42] J. Larsson, S. Kawai, J. Bodart *et al.*, Large eddy simulation with modeled wall-stress: Recent progress and future directions, Mech. Eng. Rev. **3**, 15-00418 (2016).

[43] S. Kawai and K. Asada, Wall-modeled large-eddy simulation of high Reynolds number flow around an airfoil near stall condition, Comput. Fluids **85**, 105 (2013).

[44] J. Pantaleone and J. Messer, The added mass of a spherical projectile, Am. J. Phys. **79**, 1202 (2011).

[45] T. T. Truscott, B. P. Epps, and A. H. Techet, Unsteady forces on spheres during free-surface water entry, J. Fluid Mech. **704**, 173 (2012).

[46] P. A. Tyvand and T. Miloh, Free-surface flow due to impulsive motion of a submerged circular cylinder, J. Fluid Mech. **286**, 67 (1995).

[47] A. Sareen, J. Zhao, J. Sheridan *et al.*, Vortex-induced vibrations of a sphere close to a free surface, J. Fluid Mech. **846**, 1023 (2018).

[48] S. Ohring and H. J. Lugt, Interaction of an obliquely rising vortex ring with a free surface in a viscous fluid, Meccanica **31**, 623 (1996).

[49] S. Kara, M. C. Kara, T. Stoesser *et al.*, Free-surface versus rigid-lid LES computations for bridge-abutment flow, J. Hydraul. Eng. **141**, 04015019 (2015).

[50] F. Alzabari, C. A. M. E. Wilson, and P. Ouro, Unsteady vortex shedding dynamics behind a circular cylinder in very shallow free-surface flows, Comput. Fluids **260**, 105918 (2023).

[51] M. M. Rajamuni, K. Hourigan, and M. C. Thompson, Vortex-induced vibration of a sphere close to or piercing a free surface, J. Fluid Mech. **929**, A41 (2021).

[52] V. P. Ruban, Interaction of a vortex ring with the free surface of an ideal fluid, Phys. Rev. E **62**, 4950 (2000).

[53] M. Song, Hydrodynamic study of water entry and exit phenomena, Ph.D. thesis, University of Michigan, 1991.